Improved laser absorption spectroscopy measurements of flame temperature via a collisional line-mixing model for CO_2 spectra near 4.17 µm

Mingming Gu[1] · Shaojie Wang[1] · Guoqing Wang[1] · Qiuxiao Wang[1] · Xunchen Liu[1] · Fei Qi[1] ·
Christopher S. Goldenstein[2]

Abstract

An experimental and theoretical study of CO_2 absorption spectroscopy near 4.172 µm was conducted to acquire measurements of gas temperature and CO_2 concentration in flames at near-atmospheric pressure. Scanned-wavelength laser absorption spectroscopy measurements were obtained in laminar non-premixed flames produced using either a Hencken burner or inside a fixed-volume combustion vessel. For the Hencken burner flame, the non-uniform distribution of gas conditions along the line-of-sight was estimated from computational fluid dynamics (CFD) simulations and accounted for in simulations of path-integrated absorbance spectra. Gas properties were inferred from measured absorbance spectra using two models: (1) an isolated line model employing the Voigt Profile and (2) a collisional line-mixing model. Regarding the latter, the relaxation matrix for CO_2 in the line-mixing model was modified and scaled based on an empirically derived collisional-relaxation matrix for CO_2–Ar. The collisional line-mixing model reduced the residuals of the best-fit spectra by approximately a factor of 4. In addition, the flame temperature obtained from the line-mixing model agreed well with that predicted by adiabatic equilibrium calculations and was typically 10% more accurate than those produced by the isolated line model, thereby illustrating the importance of accounting for collisional line mixing at the conditions and wavelengths studied despite the modest gas pressure and high temperature.

1 Introduction

Carbon dioxide (CO_2) is a major product of hydrocarbon fuels and is, therefore, an attractive candidate for providing temperature measurements in combustion environments using laser absorption spectroscopy. Previously, CO_2 absorption measurements were primarily conducted using transitions in the near-infrared. This includes measurements in the $(0,0^0,0 \rightarrow 2,2^0,1)$ vibrational band near 1.5 µm [1], as well as in the $(0,0^0,0 \rightarrow 1,2^0,1)$ vibrational band near 2.0 µm [2–4]. The advent of tunable diode lasers in the extended near-infrared (2.7 µm) has enabled absorption measurements with significantly larger signal levels, for example,

measurements in the $(0,0^0,0 \rightarrow 1,0^0,1)$ and $(0,0^0,0 \rightarrow 0,2^0,1)$ combination bands have demonstrated much better signal-to-noise ratio, especially for high-temperature combustion applications [5–7]. Perhaps more significantly, the development of interband cascade lasers (ICL) and quantum cascade lasers (QCL) has provided access to even stronger absorption transitions in the mid-infrared. For example, the R(76) transition in the $(0,0^0,0 \rightarrow 0,0^0,1)$ fundamental band transition near 4.3 µm was used for sensitive CO_2 concentration measurements during thermal decomposition of C3–C5 ethyl esters by Ren et al. [8] using an external cavity QCL. In addition, Spearrin et al. measured the concentration of CO_2 in a scramjet combustor at the same wavelength [9].

More recently, absorption measurements near the $(0,0^0,0 \rightarrow 0,0^0,1)$ bandhead at 4.172 µm have become popular due to the good signal-to-noise ratio, high temperature sensitivity and isolation from interfering absorption lines of, for example, H_2O [10]. Temperature measurements in flames at the $(0,0^0,0 \rightarrow 0,0^0,1)$ bandhead were first demonstrated by Villareal et al. [11] on a McKenna burner and was latter demonstrated in several different combustion

✉ Mingming Gu
minggu163@sjtu.edu.cn

1 School of Mechanical Engineering, Shanghai Jiao Tong University, Shanghai 200240, China

2 School of Mechanical Engineering, Purdue University, West Lafayette, IN 47906, USA

facilities [12–14]. Accurate flame thermometry was also obtained by scanning across multiple absorption transitions within the $(0,0^0,0 \rightarrow 0,0^0,1)$ band [10, 14–16] or by combining simultaneous measurements in the $(0,0^0,0 \rightarrow 0,0^0,1)$ band and the $(0,0^0,0 \rightarrow 0,2^0,1)$ combination band [17]. In many of the aforementioned studies [12, 13], however, simulated spectra performed using an isolated line model and the HITEMP [18] database did not produce satisfactory agreement with the experimentally measured spectra, and gas-cell experiments were needed to correct the line positions and line intensities. Some authors pointed out that the possible cause for poor agreement could be collisional line-mixing effects [13].

Collisional line-mixing (LM) results from collision-induced transfer of rotational state populations and it can cause absorption to shift from the wings to the center of a vibrational band. Collisional line mixing is most significant when the collisional linewidth is comparable to the spacing of the rotational lines. This occurs when the gas number density or collision frequency is high, and/or when the rotational lines are tightly spaced, for example, near bandheads. Conventionally, collisional line-mixing effects are often only considered important at high pressures. In this work, we show that collisional line mixing has a significant impact on the absorbance spectrum of CO_2's v_3 fundamental band near the bandhead in atmospheric pressure flames.

For CO_2, many studies have been devoted to developing databases for the collisional-broadening coefficients among different collisional partners while accounting for collisional line mixing. For example, those gaseous species include, but are not limited to O_2, CO_2, N_2 [19–21] as well as by noble gases like Ar [21–25]. Among those studies, Brownsword et al. [23] concluded that the J-dependent collisional linewidths for CO_2–Ar and CO_2–N_2 differed only by a scalar and the dependence of the collisional linewidth on the vibrational band was negligible. This indicates that the same set of collisional-broadening coefficients can be applied to both Raman and absorption spectroscopy calculations for different bands. On the other hand, many studies have been devoted to developing semi-empirical scaling laws [24, 26–30] or by performing ab initio calculations [31–35] to compute the state-to-state collision rate and, thus, the collisional-broadening coefficient for CO_2–CO_2 collisions or for CO_2–Ar collisions. There are also some databases that can provide necessary parameters for CO_2 absorbance calculations that account for collisional line mixing [36].

However, direct experimental measurements and validation of CO_2 line-mixing parameters at combustion relevant conditions are rare. Recently, Lee et al. [37, 38] first reported measurements of the CO_2–Ar collisional linewidth for absorption transitions near 4.172 μm which correspond to rotational levels $J = 99$–145. The authors acquired such measurements in a shock tube in CO_2–Ar mixtures at temperatures up to 3000 K. They also empirically derived the scaling coefficients for the Modified exponential Energy Gap (MEG) law to calculate the J-dependent CO_2–Ar state-to-state collision rate. Their model covered all the major absorption lines at and near the bandhead and showed excellent agreement between measured and modeled spectra at pressures up to 58 atm. In addition, they modified the collisional line-mixing model extracted from the CO_2–Ar measurements by a scaling constant to apply it to more practical situations such as inside a rotating detonation engine [39]. The spectral-fitting results were satisfactory and were greatly improved over those produced using an isolated line model with the Voigt profile. However, the gaseous compositions in practical combustion applications are usually more complex than in a shock tube. In addition, it is difficult to rigorously evaluate the accuracy of temperature measurements obtained in detonation engines.

In this work, we demonstrate that accounting for collisional line mixing not only improves residuals between measured and modeled CO_2 absorbance spectra near 4.172 μm but also gives more accurate thermometry measurements in several near-atmospheric pressure flames. The experimental measurements were performed in a laminar non-premixed flame established over a Hencken burner as well as a spherically expanding flame established inside a fixed-volume combustion vessel. The measured flame temperatures in both of those two test facilities were close to their adiabatic values. For Hencken burner flames, the effects of non-uniform distribution of flame properties were accounted through CFD simulations. A Boltzmann profile [16, 40] was assumed for flame temperature and CO_2 concentration distributions along the line-of-sight in calculating path-integrated absorbance spectra. A collisional line-mixing model was implemented using the G-matrix method. The collisional-relaxation matrix was adjusted by scaling the empirically derived collision rate for CO_2–Ar model [37] with a scalar that was inferred from the measured spectra using a similar, but different approach to Nair et al. [39]. The results illustrate that this approach provides improved thermometry measurements even when the gaseous mixtures are not known a priori. The validity of this approach is discussed in detail later.

2 Experimental setup

2.1 Optical equipment

Figure 1 shows a schematic of the experimental setup. A continuous-wave distributed-feedback (DFB) interband-cascade laser (ICL) with a center wavelength of 4.172 μm (Nanoplus) was used for all measurements. The function generator (Tektronix AFG3022C) was used to generate
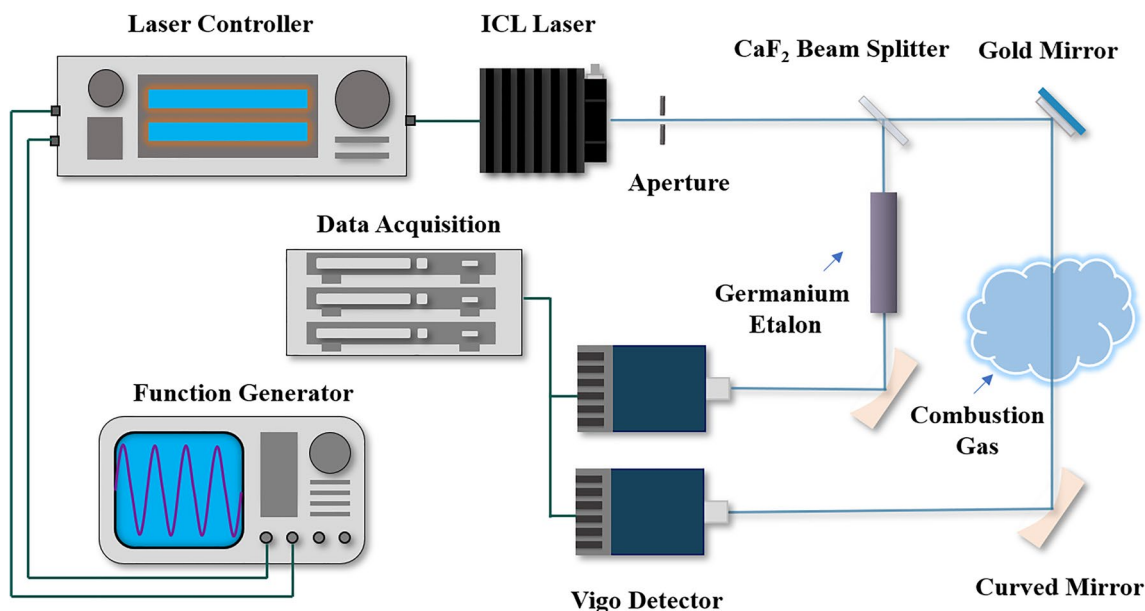
Fig. 1 Schematic of the experimental setup used to characterize burner flames with laser-absorption measurements of CO_2 near 4.172 μm

10 kHz triangle waveforms that were input into the laser diode controller (Stanford Research System, LDTC0520) to scan the injection current of the ICL. A CaF_2 beamsplitter was used to create a second beam which was passed through a Germanium etalon to characterize how the relative frequency of the laser varied throughout each scan, the absolute frequencies, on the other hand, could be determined by comparing the absorption features to numerical simulations. The free spectral range (FSR) of the etalon used in this work is 0.012 cm^{-1}. The laser intensity was measured by two thermoelectrically cooled mercury cadmium telluride (MCT) photovoltaic detectors (PVI-3TE, Vigo System).

3 Combustion equipment

Flame temperature measurements were acquired in both laminar non-premixed flames and laminar premixed flames. The laminar non-premixed flame was produced using a Hencken burner, and previous studies have shown that with sufficiently high flow rate, the heat loss to the burner is insignificant and the flame temperature at 0.8–3 cm above the burner surface is approximately the adiabatic flame temperature for H_2-Air and CH_4-Air flames [41, 42]. Figure 2 shows a schematic of the homemade
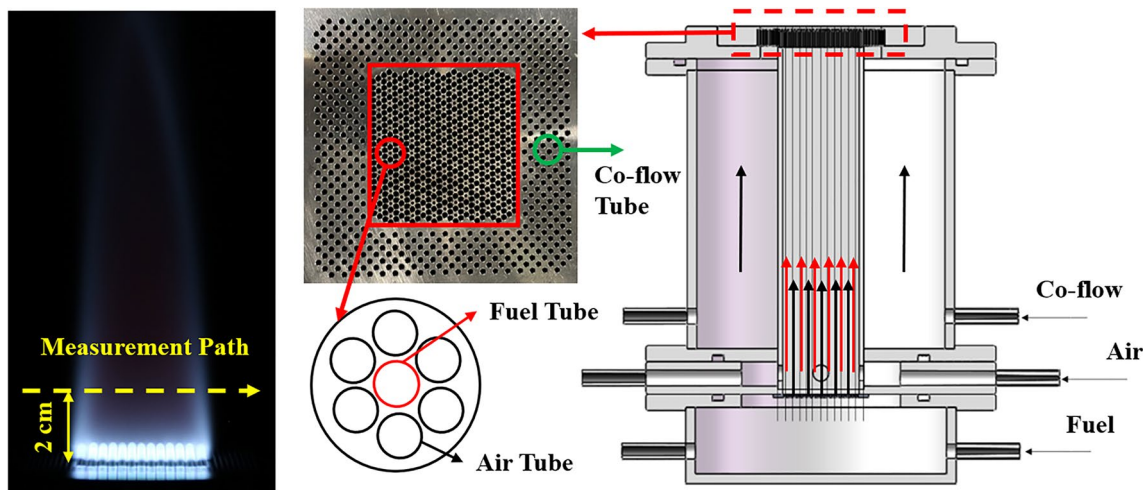
Fig. 2 Schematic of the Hencken burner used to produce laminar non-premixed flames

Hencken burner. The laser beam was passed 2 cm above the burner surface where the flames were stable and the flame temperature was near equal to the adiabatic flame temperature.

A CFD simulation was performed with the kinetic model developed by Qi et al. [43] for DME–air flames to estimate and account for the impact of the non-uniform distributions of flame temperature and CO_2 concentration on measurement accuracy. The air flow rate was set as 15 standard liter per minute (SLM), while the co-flow N_2 flow rate was set as 10 SLM to be consistent with the experimental condition. The fuel and the oxidizer are sufficiently mixed within less than one millimeter above the burner surface, and the regime of interest in this work is at 2 cm above the burner. Thus, we simplified the dense distributions of the fuel tubes and air tubes and treated the burner geometry as a 25.4 mm diameter tube where the reactants are fully premixed. This treatment was also used in some previous numerical studies of Hencken burner flame structure, and good agreement between the simulation and the experimental measurements were reported [44, 45]. An example of two-dimensional temperature and CO_2 mole fraction distributions provided by CFD for the stoichiometric DME–air flame are shown in Fig. 3

As is shown in Fig. 3, the temperature and CO_2 concentration profiles are uniform along the optical path in the core of the Hencken flame. The boundary layers can be modeled using the simplified 2-T/trapezoid profile [46] or more realistic Boltzmann profile [16, 40]. In this work, the Boltzmann profile in the form of Eq. (1) was used to model the flame temperature and CO_2 concentration distribution in path-integrated absorbance calculations. In Eq. (1), y denotes the physical property (temperature or CO_2

concentration), x represents the spatial location along the line-of-sight, $C_{1,y}$ and $C_{2,y}$ are the values of the physical properties in the flame core (determined from spectral fitting to absorbance spectra) and the ambient condition ($C_{2,T} = 300$ K, $C_{2,x} = 700$ ppm), respectively, C_3 is the spatial location where the flame temperature or concentration is equal to $\frac{C_{1,y} + C_{2,y}}{2}$ and $\frac{1}{C_4}$ is to characterize the gradient of the flame periphery. Both C_3 and C_4 can be inferred from the CFD simulation. For example, for the flame condition shown in Fig. 3, $C_{3,T} = 1.4$ cm, $C_{4,T} = 0.23$ cm and $C_{3,X} = 1.35$ cm, $C_{4,X} = 0.2$ cm.

$$y = C_{2,y} + \frac{C_{1,y} - C_{2,y}}{1 + \exp\left(\frac{x - C_3}{C_4}\right)}. \tag{1}$$

The laminar premixed flame studied was a spherically expanding flame which was generated inside a fixed-volume combustion vessel [47, 48] since this vessel has been widely used to study laminar burning velocities. In this work, ethylene–air mixtures were ignited at the center of the combustion vessel at atmospheric pressure. The combustion process and the subsequent expansion of the flame causes the pressure to rise which was characterized using a pressure transducer. In addition, a high-speed camera was used to monitor the flame expansion to provide time-resolved measurements of the flame diameter (i.e., the absorbing path length).

Fig. 3 CFD calculation of the **a** CO_2 concentration and **b** temperature distribution for DME–Air Hencken burner flame for stoichiometric conditions. Only one half of the flame is shown because it is center-symmetric
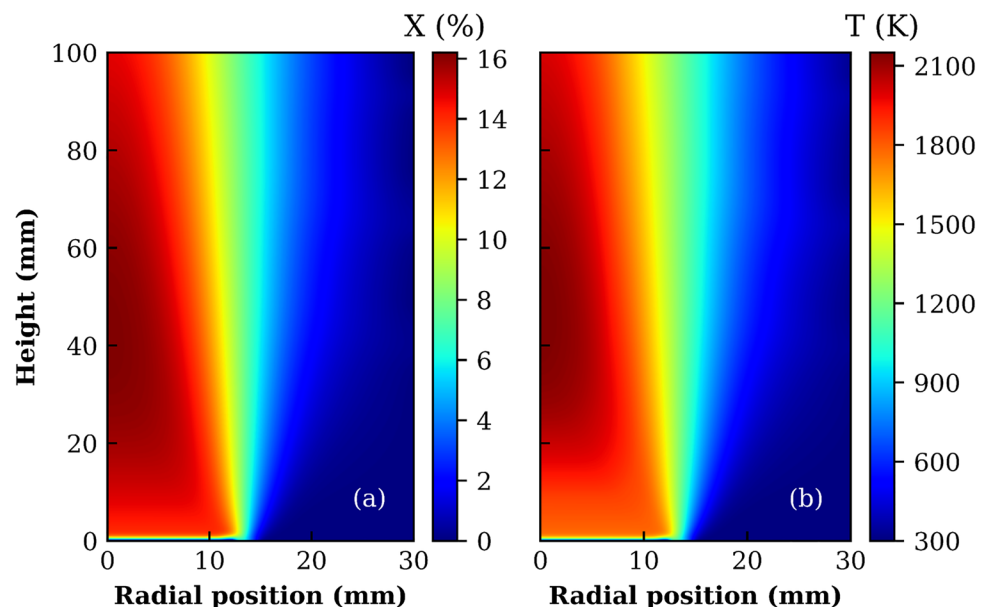
4 Theory of absorption spectroscopy

4.1 Isolated line model

At low to moderate densities, the isolated line approximation is typically extremely accurate and the absorbance spectrum of a given molecule can be calculated for a non-uniform line-of-sight using Eq. (2).

$$\alpha(\nu - \nu_0) = \int_0^L n X_{\text{abs}}(x) \cdot \sum_i S_i(T(x)) \phi_i(\nu - \nu_0, \Delta\nu_{\text{D}}, \Delta\nu_{\text{C}}) \mathrm{d}x. \tag{2}$$

Here, the subscript i denotes a given absorption transition, L(cm) is the entire absorbing path length and x is the position variable representing the location along the LOS, n(mol·cm^{-3}) is the total gas number density and $X_{\text{abs}}(x)$ and $T(x)$ are the spatially dependent mole fraction and temperature of the absorbing species and are given in the form of Eq. (1), $S_i(T)$ (cm^{-1}/mol·cm^{-2}) is the transition line strength, and ϕ_i (cm) is the transition lineshape function. The Voigt profile is very commonly used to model the transition lineshape and it is given by the convolution of the Gaussian profile $G(\nu', \Delta\nu_{\text{D}})$ and Lorentzian profile $L(\nu', \Delta\nu_{\text{C}})$:

$$\phi(\nu', \Delta\nu_{\text{D}}, \Delta\nu_{\text{C}}) = \int_{-\infty}^{+\infty} G(\nu'', \Delta\nu_{\text{D}}) L(\nu' - \nu'', \Delta\nu_{\text{C}}) \mathrm{d}\nu'', \tag{3}$$

where ν' is the relative wavenumber with regard to the transition linecenter ν_0 (cm^{-1}), $\Delta\nu_{\text{D}}$ (cm^{-1}) and $\Delta\nu_{\text{C}}$ (cm^{-1}) are the Doppler full-width at half-maximum (FWHM) and collisional FWHM, respectively.

4.2 Line-mixing model

At high density or for densely packed transitions, collisional coupling (i.e., line mixing) can have a large impact on a molecule's absorbance spectrum and, thus, the isolated line approximation is no longer accurate. In this case, the so-called G-matrix formula can be used to calculate the absorbance spectrum using Eq. (4) for a non-uniform line-of-sight:

$$\alpha(\nu) = \int_0^L \frac{n X_{\text{abs}}(x)}{\pi} \text{Im}\left(\mathbf{d} \cdot \tilde{\mathbf{G}}^{-1}(\nu) \cdot \tilde{\boldsymbol{\rho}} \cdot \mathbf{d}^T\right) \mathrm{d}x, \tag{4}$$

where $\tilde{\boldsymbol{\rho}}$ is a $N \times N$ diagonal matrix where N is the number of absorption transitions. The diagonal elements of $\tilde{\boldsymbol{\rho}}$, ρ_i, are given by the Boltzmann population fraction of the lower state of the transition and its off-diagonal elements are set to zero. The row vector $\mathbf{d}$ and its transpose $\mathbf{d}^T$ represent the transition amplitude, with its element given by Eq. (5).

$$d_i = \sqrt{\frac{S_i(T(x))}{\rho_i}}. \tag{5}$$

The matrix $\tilde{\mathbf{G}}$ accounts for the collisional broadening and line mixing and can be given as:

$$G(\nu) = \nu\tilde{\mathbf{I}} - \tilde{\boldsymbol{\nu}}_0 + iP\tilde{\mathbf{W}}, \tag{6}$$

where $\tilde{\mathbf{I}}$ is the $N \times N$ identity matrix, $\tilde{\boldsymbol{\nu}}_0$ is a diagonal matrix with its nonzero element $\nu_{0,i}$ (cm^{-1}) corresponding to the transition frequencies, P (atm) is the pressure, and $\tilde{\mathbf{W}}$ is the collisional-relaxation matrix where its diagonal and off-diagonal elements are given by Eq. (7).

$$W_{ij} = \begin{cases} \gamma_i - i\delta_i, & i = j \\ R_{ij}, & i \neq j. \end{cases} \tag{7}$$

The subscripts i and j denote the rotational quantum numbers. The diagonal elements of Eq. (7) $\gamma_i - i\delta_i$ were taken from the HITEMP database [18]. The off-diagonal elements of W_{ij} correspond to the state-to-state collision rate. The collision rate is provided by the modified exponential energy gap (MEG) law as shown in Eq. (8).

$$R_{ij} = a_1(T) \left[\frac{1 + a_4\left(\frac{E_i''}{a_2 k_{\text{B}} T}\right)}{1 + a_4\left(\frac{E_i''}{k_{\text{B}} T}\right)} \right] \times \exp\left[\frac{-a_3\left(E_j'' - E_i''\right)}{k_{\text{B}} T} \right]. \tag{8}$$

The collisional-broadening coefficients and the MEG law coefficients used here were taken from Lee et al.[37] which are strictly valid for the CO_2–Ar collision system. In flames, the compositions of gaseous species are much more complex. As a result, in this work the collision rate obtained from the CO_2–Ar system was scaled by an empirically derived scaling constant, k, according to Eq. (9).

$$\tilde{\mathbf{W}}_{CO_2\text{-mix}}(T) = \tilde{\mathbf{W}}_{CO_2\text{-Ar}}(T) \cdot k = \tilde{\mathbf{W}}_{CO_2\text{-Ar}}(T) \left(\frac{\gamma_{CO_2\text{-mix}}(T)}{\gamma_{CO_2\text{-Ar}}(T)} \right), \tag{9}$$

$$\gamma_{CO_2\text{-mix}} = \sum_B X_B \gamma_{CO_2-B}. \tag{10}$$

The subscript CO_2–B denotes the collision partner between CO_2 and an arbitrary gaseous species B, X_B is its corresponding mole fraction. It should be noted that in Eqs. (9) and (10), the species-specific collisional-broadening coefficient is also rotational-level (i.e., state) dependent. Ideally, Eqs. (9) and (10) should be evaluated for all the relevant rotational levels. Unfortunately, a thorough and experimentally verified database of collisional-broadening parameters between CO_2 and major combustion species like N_2, O_2, H_2O, etc. is currently unavailable especially for high rotational quantum numbers. In the

work by Nair et al. [39], γ_{CO_2-B} in Eq. (10) was referenced to the $J'' = 100$ transition and the collisional-broadening coefficients for CO_2 colliding with several major combustion species were provided by Rosenmann et al. [49]. This can be justified by the fact that at high temperatures, the broadening coefficients between CO_2 and other gaseous species are weakly dependent on J [50, 51]. In this work, we further took advantage of this approximation and chose using the J-averaged collisional-broadening coefficient to calculate the scaling parameter k as the initial guess for the relaxation matrix calculation for several flame gases and conditions [49].

$$\overline{\gamma}(T) = \sum_{i=0}^{J_{max}} \rho_i \gamma_i(T), \tag{11}$$

where ρ_i is the fractional population in the rotational level i according to the Boltzmann distribution, and γ_i is the corresponding broadening coefficient.
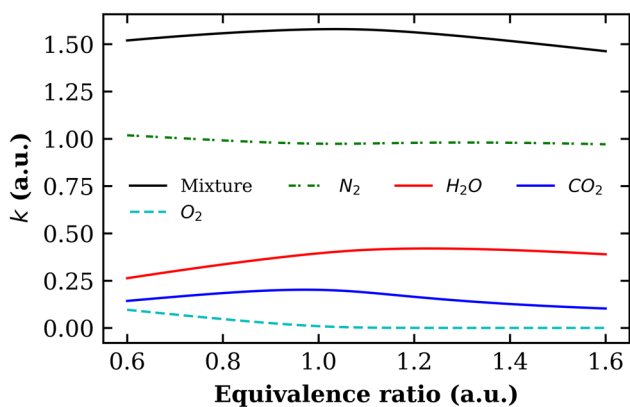
Figure 4 shows how $k = X_B \cdot \gamma_{CO_2-B}/\gamma_{CO_2\text{ - Ar}}$ varies with equivalence ratio for several collision partners and a mixture of collision partners corresponding to premixed DME–air flame gas at equilibrium. The gaseous compositions and the temperatures were calculated assuming at constant enthalpy and pressure condition. It can be concluded from Fig. 4 that k does not vary significantly with the equivalence ratios for the mixture, this is largely due to the fact that the collisional rates for CO_2–Ar and CO_2–N_2 systems are highly alike [28]. To account for the uncertainties from inexact gas compositions and from the calculated collisional-broadening coefficients etc., in this work, we set k as a free parameter in the spectral-fitting routine used for data processing and the calculations based on Eqs. (9)–(11) were only used as the initial guess value for k in the spectral-fitting routine. We will also show how different values of k affect the best-fit temperatures in Sect. 4.3.

5 Results and discussion

5.1 Preprocessing

Figure 5 shows example single-scan measurements of I_o, I_t, and the corresponding CO_2 absorbance spectrum. I_o was recorded before each measurement. To mitigate the impact of beam steering induced by the flame, I_o was recorded in the open air as well as in H_2–Air flames at different equivalence ratios. An example measurement of I_o is shown in Fig. 5b which illustrates that I_o was not significantly impacted by the flame. In addition, Fig. 5a and c shows that CO_2 absorption near 4.172 µm is very weak at room temperature, indicating the ambient absorption has negligible effects on the baseline and flame measurements.

Fig. 4 Value of k for various collision partners or a mixture of collision partners corresponding to DME–air flame as a function of equivalence ratio. Note, the value of k varies with equivalence ratio for a single collision partner due to the temperature and concentration varying
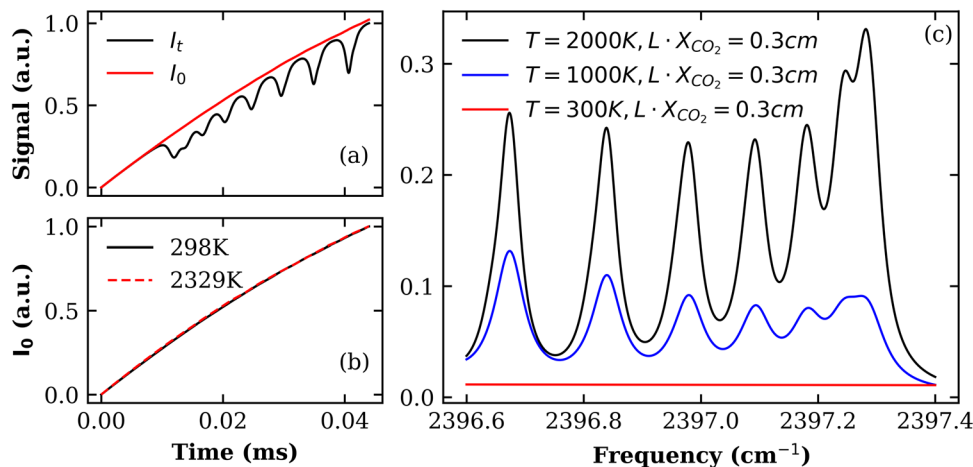
Fig. 5 **a** Example of the measured transmitted light intensity I_t and the unabsorbed background I_0. **b** Measured unabsorbed background signal in the open air (solid line) and in the stoichiometric H_2–Air flame (dash line). **c** Simulated absorbance spectrum based on HITEMP database and Voigt profile

5.2 Spectral-fitting routine

The spectral-fitting routine is described as follows. The experimentally measured spectra were preprocessed as described in Sect. 4.1. We used the profile-fitting strategy as introduced in Eqs. (2) and (4) to account for the spatial inhomogeneity in Hencken burner flames. The temperature and species concentration profiles were given in the form of Eq. (1) and $C_{1,T}$ and $C_{1,X}$ (the values of temperature and CO_2 mole fraction in the flame core) were determined from the spectral-fitting routine. Parameters like $C_{2,T}$ and $C_{2,X}$ were pre-set ($C_{2,T} = 300$ K, $C_{2,x} = 700$ ppm), while $C_{3,T}$,$C_{3,X}$ and $C_{4,T}$, $C_{4,X}$ were inferred from the CFD simulation. For the isolated line model, the theoretical spectra were calculated according to Eqs. (2) and (3). For the line-mixing model, the theoretical spectra were generated according to Eqs. (4)–(10). The transition linestrength, $S_i(T)$, and the unperturbed transition frequency $\nu_{0,i}$ were taken from the HITEMP database [18]. The collisional linewidth γ_i for CO_2–Ar and the off-diagonal collisional rates R_{ij} were taken from Lee et al. [37]. The temperature ($C_{1,T}$), CO_2 concentration ($C_{1,X}$), the scaling parameter k of the relaxation matrix were set as free parameters in the spectral-fitting routine. In addition, a wavelength shift parameter and a baseline shift parameter for correcting I_o were included in the line-mixing model as well

Table 1 Summary of free parameters used in the spectral-fitting routine

| Fitting parameter	Floating range
Concentration ($C_{1,X}$)	5 to 20%
Temperature ($C_{1,T}$)	1200 to 2800 K
Pressure	0.95 to 1.05 atm
Wavelength shift parameter	− 0.02 to 0.02 nm
Baseline shift parameter	− 0.05 to 0.05
k(line-mixing calculation only)	1.5 to 2.5

as the isolated line model. A summary of the free parameters used in the spectral-fitting routine is shown in Table 1.

For each dataset, the best-fit spectrum for the first scan/measurement was fitted using the brute-force search combined with the Broyden–Fletcher–Goldfarb–Shanno (BFGS) method [52] to ensure that the fitting routine converged on the global minimum. After that, the best-fit values for each free parameter was used as the initial guess values for each consecutive measurement and the least-squares method was used to find the best-fit parameters. This is to reduce the load of numerical calculations as well as to find the global optimum solution.

5.3 Hencken burner flame

Laser-absorption measurements were first acquired in a laminar non-premixed DME–air flame. The volumetric flow rate of the air was set at 15 standard liter per minute (SLM) so that the overall speed of the fuel–air mixture was slightly higher than the laminar flame speed of DME at the stoichiometric combustion condition. An example of the measured CO_2 absorbance spectrum compared to best-fit spectra obtained using the conventional isolated line model (i.e., Voigt model) and the line-mixing (LM) model are shown in Fig. 6. The agreement between the measured and best-fit spectra is much better for the line-mixing model than the isolated line model, especially at the bandhead where the transitions overlap most significantly, the overall relative fitting residual from the isolated line model (15%) is about 3 times larger than from the line-mixing model (4%). In addition, we also compared the spectral-fitting results obtained with LM model and by assuming a uniform distribution of flame temperature and CO_2 concentration (denoted as LM2) in Fig. 6b. The best-fit spectra were not significantly different between two assumptions; however, the fitting accuracy was slightly improved near the absorption bandhead using the non-uniform temperature and CO_2 concentration profile

Fig. 6 Comparisons of best-fit absorbance spectra for the same experimental data obtained using **a** the isolated line model and **b** the line-mixing model, both of which account for line-of-sight non-uniformities. LM2 denotes the best-fit from assuming uniform distribution of flame temperature and CO_2 concentration along the line-of-sight with an optical path length of 2.54 cm. The measurement was performed in a stoichiometric DME–air flame and the experimental spectra was averaged over 100 consecutive scans
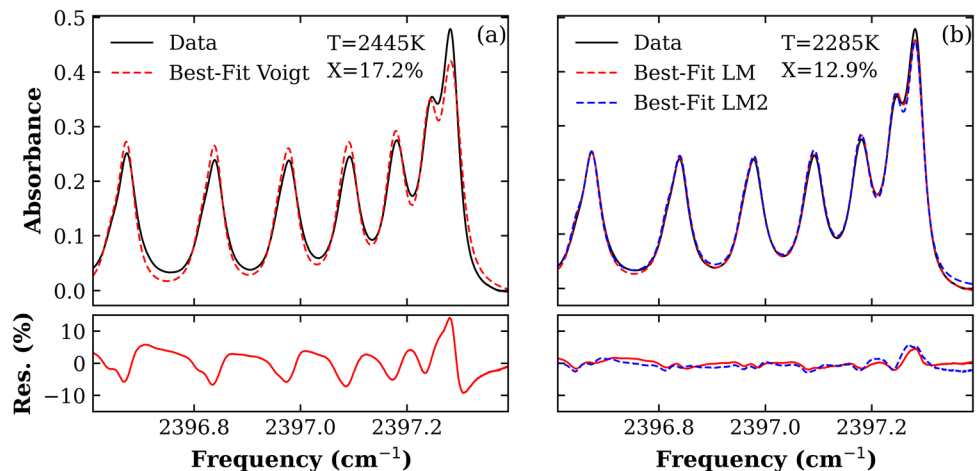
Fig. 7 Summary of **a** measured core flame temperature ($C_{l,T}$) and **b** core CO_2 mole fractions ($C_{l,X}$) for DME–air flames with various equivalence ratio acquired using the line-mixing model or the Voigt model
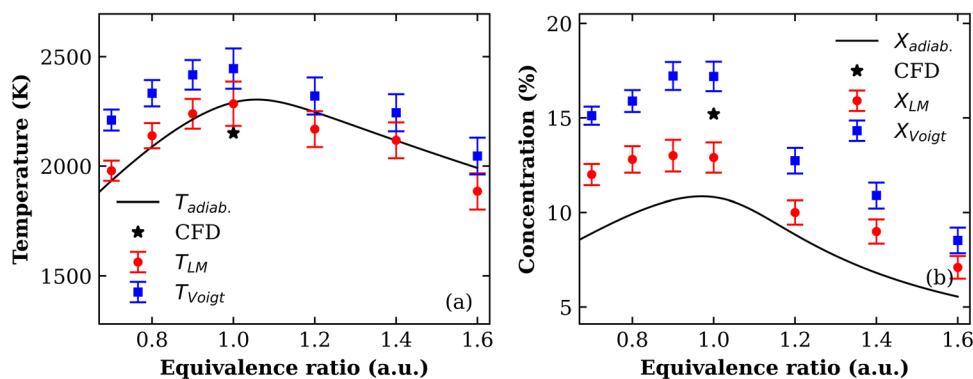
as inferred from CFD calculations. Further, based on the uniform flame property assumption, the best-fit temperature $T_{LM2} = 2217$ K was slightly lower than $T_{LM} = 2285$ K and the best-fit concentration $X_{LM2} = 13.8\%$ was higher than $X_{LM} = 12.9\%$.

In addition, Fig. 7 shows a comparison of the measured core flame temperature obtained using the two models at various equivalence ratios. The adiabatic flame temperature was calculated assuming chemical equilibrium using Cantera [53] with the kinetic model developed by Qi et al. [43]. For the stoichiometric combustion condition, the flame temperature and CO_2 mole fraction in the flame core obtained from CFD simulations are also shown.

In Fig. 7, the error bar was evaluated based on the standard deviation from the 100 measured spectra acquired at 10 kHz rate as well as the uncertainty from the spectral-fitting routine, the magnitude of the error bar was 40–120 K for flame temperature and 0.5–0.8% for CO_2 mole fraction measurement and for equivalence ratios from 0.7 to 1.6. The absolute uncertainty of flame temperature, on the other hand, was about 30–80 K as estimated from previous femtosecond CARS measurement [54, 55]. For all the flame conditions studied, the temperature measured using the Voigt model were about 100–200 K higher than those obtained using the line-mixing model. This is caused by the fact that Voigt model underestimates the absorbance at the bandhead. For stoichiometric combustion condition, the flame core

temperature from CFD calculation was 140 K lower than adiabatic flame temperature, this is caused by the fact that heat loss due to radiation and convection were considered in the CFD simulation. The agreement between the temperature obtained using the line-mixing model and the adiabatic temperature were in general satisfactory except at high equivalence ratios. For the fuel rich conditions, the measured temperatures obtained using the line-mixing model are 50–125 K lower than the adiabatic flame temperatures. The behavior was also found in other studies investigating fuel rich flames with carbonaceous fuels [56, 57] and is attributed to the radiative heat loss from soot. The best-fit CO_2 mole fractions from line-mixing calculations are 1–3% higher than the adiabatic equilibrium. On the other hand, at stoichiometric combustion condition, the best-fit CO_2 mole fraction is 2% lower than it was obtained from the CFD calculations. Considering the fact that many previous studies have shown that the experimentally measured flame temperatures were usually only 30–80 K lower than their adiabatic values [54, 55], it is likely that our current CFD calculation could overestimate the heat loss due to radiation and convection. While the adiabatic equilibrium calculations do not consider heat loss, it is reasonable to infer that the real flame temperatures and CO_2 concentrations were in between the values obtained from CFD simulation and adiabatic calculations as indicated by the laser absorption measurements.

Fig. 8 a The experimentally fitted scaling parameter k for the collisional coefficient as compared to the scaling parameters calculated from J-averaged collisional-broadening coefficient and from the collisional-broadening coefficient referenced from $J = 100$. **b** The best-fit temperatures corresponding to different values of k. The results shown are for DME–air flames
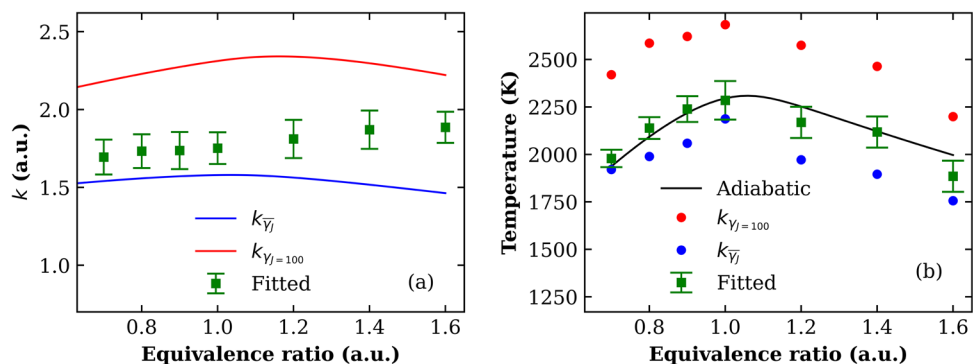
To better understand the accuracy of the line-mixing model, we compared the best-fit value of k with that predicted by two models. Figure 8a shows how the measured and predicted values of k differ as a function of equivalence ratio. The difference between the best-fit (i.e., fitted) k and the theoretical predictions is not surprising, considering the fact that the J-dependencies cannot be totally neglected. In addition, there are some studies showing discrepancies between the experimentally measured linewidth and those predicted by the calculations proposed by Rosenman et al. [58].
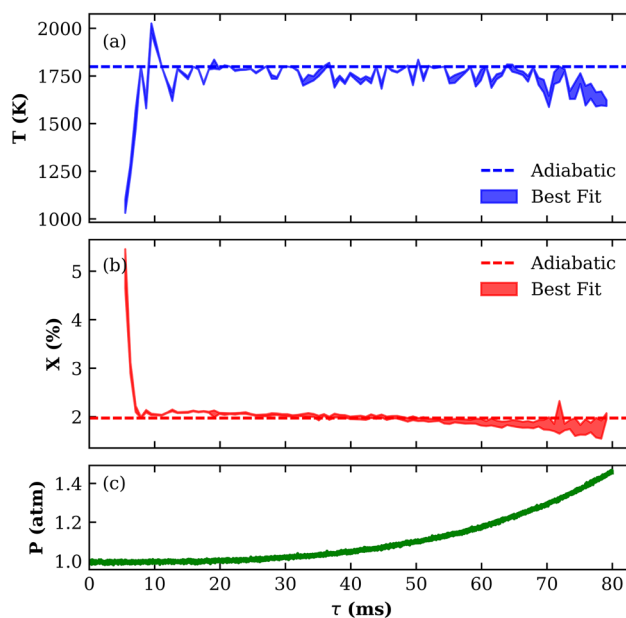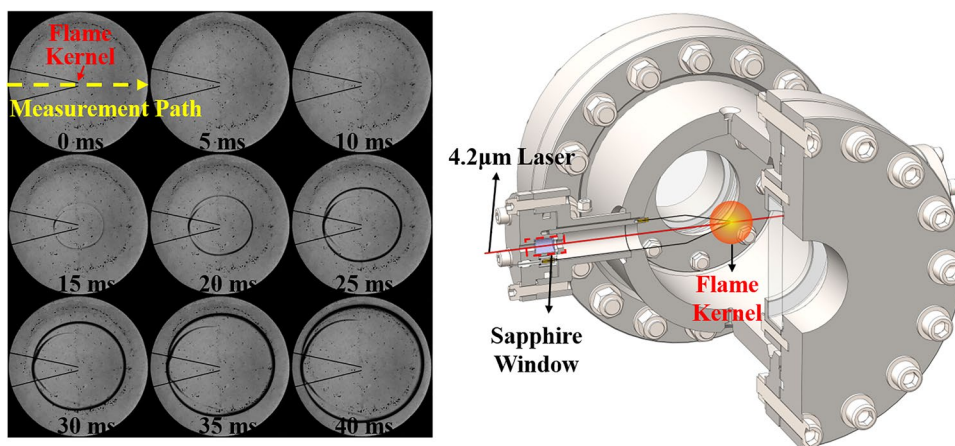
Figure 8b illustrates how the measured temperature varies with equivalence ratio and with the method for determining k (inferring it or fixing it to different predicted values). Increasing or decreasing k leads to the same trend in temperature. While there is significant uncertainty in the most accurate value for k and how to infer or predict it, it is clear that direct determination of the collisional-relaxation matrix for each mixture can help increase the accuracy of the temperature measured using the line-mixing model.

5.4 Spherical flame inside constant-volume combustion vessel

Inside the fixed-volume combustion vessel, the pressure was monitored using a pressure transducer. In the experiment, an ethylene–air mixture with an equivalence ratio of 2.2 was first ignited in the center of the combustion vessel with the gas initially at 1 atm. The combustion process then caused the pressure to increase throughout the test. The pressure measured by the transducer was used as an input to the spectral-fitting routine. The optical path length through the spherical flame can be precisely determined through high-speed imaging as shown in Fig. 9. Measured time histories of temperature, CO_2 concentration and pressure are shown in Fig. 10.

The temperature rise is obvious and expected during ignition; however, the drop in CO_2 concentration might be

Fig. 10 Measured time histories of **a** the gas temperature, **b** the CO_2 concentration, and **c** the gas pressure for the ethylene–air flame inside the constant-volume combustion vessel. The temperature and concentration of CO_2 were determined using the line-mixing model. The fuel–air equivalence ratio was 2.2 and the shaded area denotes the uncertainty due to spectral-fitting routine

related to uncertainty in the flame diameter when it was small, as well as the low signal-to-noise ratio at early times. In general, the measured temperature and CO_2 concentration agree well with the adiabatic flame calculations after the flame entered a quasi-steady propagation stage.

Examples of the measured absorbance spectra and the corresponding best-fit spectra acquired during different periods of time during the spherical flame expansion are presented in Fig. 11. In general, the agreement between the measured CO_2 absorbance spectra and the best-fit spectra produced using the line-mixing model are satisfactory, particularly when the pressure is near 1 atm. The

Fig. 9 Example images of flame front and schematic of the fixed-volume combustion vessel used to generate laminar, spherically expanding, premixed flames
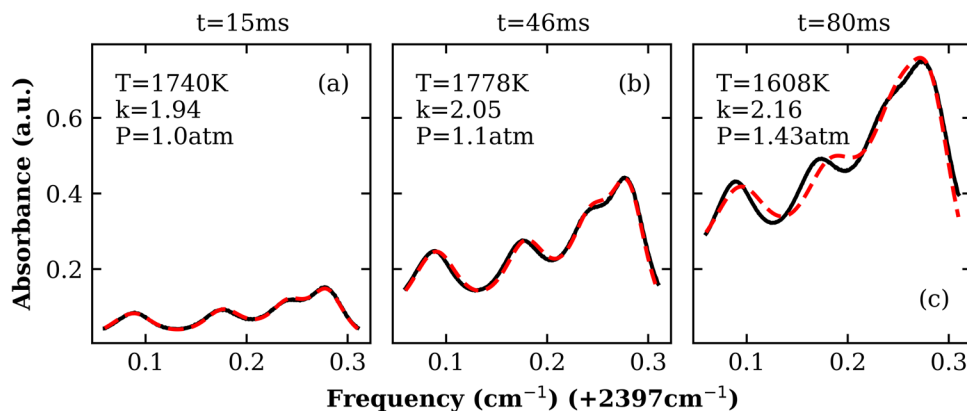
Fig. 11 Spectral-fitting results of CO_2 absorption spectra obtained using the line mixing model for spectra that were measured in the spherically expanding flame. The solid black curve denotes the experimentally measured spectra and the red dash curve represents the best-fit spectra

magnitude of the measured absorbance increases in time due to the growth of the flame. At $t = 80$ ms, differences between the experimentally measured spectra and the best-fit spectrum become more obvious than at earlier times (lower pressures). While the pressure as well as the scaling parameter increase overtime, this might indicate that the current treatment of using one single scaling parameter for the G-matrix calculation correction could fail for some intermediate pressures.

6 Conclusions

Laser absorption spectroscopy measurements of gas temperature and CO_2 concentration were acquired in laminar non-premixed flames and spherical premixed flames with varying equivalence ratio. The measurements were acquired by scanning the wavelength of a distributed-feedback inter-band-cascade laser across transitions near the bandhead of the fundamental v_3 absorption band of CO_2 near 4.17 μm. A collisional line mixing model based on previous studies of high pressure CO_2–Ar mixtures [37] was modified to provide high fidelity measurements in flames. The simulated spectra produced using the collisional line mixing model showed significantly better agreement with the experimentally measured spectra compared to simulated spectra produced using the conventional isolated line approximation and the Voigt profile. The temperature corresponding to the best-fit Voigt model significantly exceeded the values obtained using the line-mixing model, the latter of which agreed well with adiabatic equilibrium flame temperatures. As a result, this work illustrated the importance of accounting for collisional line mixing for the CO_2 transitions studied despite the modest pressure and high temperature of the flame gas. Future work will include a more accurate characterization of the collisional-broadening coefficients for different collisional species and to develop a more versatile line mixing model for low to moderately high pressures.

References

1. R.M. Mihalcea, D.S. Baer, R.K. Hanson, Diode laser sensor for measurements of CO, CO_2, and CH_4 in combustion flows. Appl. Opt. **36**(33), 8745–8752 (1997)
2. R.M. Mihalcea, D.S. Baer, R.K. Hanson, Advanced diode laser absorption sensor for in situ combustion measurements of CO_2, H_2O, and gas temperature. Symp. Int. Combust. **27**(1), 95–101 (1998)
3. M.E. Webber, J. Wang, S.T. Sanders, D.S. Baer, R.K. Hanson, In situ combustion measurements of CO, CO_2, H_2O and temperature using diode laser absorption sensors. Proc. Combust. Inst. **28**(1), 407–413 (2000)
4. J. Chen, C. Li, M. Zhou, J. Liu, R. Kan, Z. Xu, Measurement of CO_2 concentration at high-temperature based on tunable diode laser absorption spectroscopy. Infrared Phys. Technol. **80**, 131–137 (2017)
5. A. Farooq, J.B. Jeffries, R.K. Hanson, CO_2 concentration and temperature sensor for combustion gases using diode-laser absorption near 2.7 μm. Appl. Phys. B **90**(3–4), 619–628 (2008)
6. R.M. Spearrin, C.S. Goldenstein, J.B. Jeffries, R.K. Hanson, Fiber-coupled 2.7 μm laser absorption sensor for CO2 in harsh combustion environments. Meas. Sci. Technol. **24**(5), 055107 (2013)
7. A. Farooq, J.B. Jeffries, R.K. Hanson, High-pressure measurements of CO_2 absorption near 2.7μm: Line mixing and finite duration collision effects. J. Quant. Spectrosc. Radiat. Transfer **111**(7–8), 949–960 (2010)
8. W. Ren, R. Mitchell-Spearrin, D.F. Davidson, R.K. Hanson, Experimental and modeling study of the thermal decomposition of C3–C5 ethyl esters behind reflected shock waves. J. Phys. Chem. A **118**(10), 1785–1798 (2014)
9. R.M. Spearrin, C.S. Goldenstein, I.A. Schultz, J.B. Jeffries, R.K. Hanson, Simultaneous sensing of temperature, CO, and CO_2 in a scramjet combustor using quantum cascade laser absorption spectroscopy. Appl. Phys. B **117**(2), 689–698 (2014)
10. J.J. Girard, R.M. Spearrin, C.S. Goldenstein, R.K. Hanson, Compact optical probe for flame temperature and carbon dioxide using interband cascade laser absorption near 4.2 μm. Combust. Flame **178**, 158–167 (2017)

11. R. Villarreal, P.L. Varghese, Frequency-resolved absorption tomography with tunable diode lasers. Appl. Opt. **44**(31), 6786 (2005)

12. D. Wen, Y. Wang, Spatially and temporally resolved temperature measurements in counterflow flames using a single interband cascade laser. Opt. Express **28**(25), 37879 (2020)

13. X. Liu, G. Zhang, Y. Huang, Y. Wang, F. Qi, Two-dimensional temperature and carbon dioxide concentration profiles in atmospheric laminar diffusion flames measured by mid-infrared direct absorption spectroscopy at 4.2 μm. Appl. Phys. B **124**(4), 61 (2018)

14. C. Wei, D.I. Pineda, L. Paxton, F.N. Egolfopoulos, R.M. Spearrin, Mid-infrared laser absorption tomography for quantitative 2D thermochemistry measurements in premixed jet flames. Appl. Phys. B **124**(6), 123 (2018)

15. K. Wu, F. Li, X. Cheng, Y. Yang, X. Lin, Y. Xia, Sensitive detection of CO_2 concentration and temperature for hot gases using quantum-cascade laser absorption spectroscopy near 4.2 μm. Appl. Phys. B **117**(2), 659–666 (2014)

16. L.H. Ma, L.Y. Lau, W. Ren, Non-uniform temperature and species concentration measurements in a laminar flame using multi-band infrared absorption spectroscopy. Appl. Phys. B **123**(3), 83 (2017)

17. R.M. Spearrin, W. Ren, J.B. Jeffries, R.K. Hanson, Multi-band infrared CO_2 absorption sensor for sensitive temperature and species measurements in high-temperature gases. Appl. Phys. B **116**(4), 855–865 (2014)

18. L.S. Rothman, I.E. Gordon, R.J. Barber, H. Dothe, R.R. Gamache, A. Goldman, V.I. Perevalov, S.A. Tashkun, J. Tennyson, HITEMP, the high-temperature molecular spectroscopic database. J. Quant. Spectrosc. Radiat. Transfer **111**(15), 2139–2150 (2010)

19. E. Arié, N. Lacome, P. Arcas, A. Levy, Oxygen- and air-broadened linewidths of CO_2. Appl. Opt. **25**(15), 2584–2591 (1986)

20. J. Boissoles, V. Menoux, R. Le Doucen, C. Boulet, D. Robert, Collisionally induced population transfer effect in infrared absorption spectra. II. The wing of the Ar-broadened ν_3 band of CO_2. J. Chem. Phys. **91**(4), 2163–2171 (1989)

21. F. Thibault, J. Boissoles, R. Le Doucen, J.P. Bouanich, Ph. Arcas, C. Boulet, Pressure induced shifts of CO_2 lines: Measurements in the 00^03–00^00 band and theoretical analysis. J. Chem. Phys. **96**(7), 4945–4953 (1992)

22. M.S. Wooldridge, R.K. Hanson, C.T. Bowman, Argon broadening of the R(48), R(50) and R(52) lines of CO_2 in the (0001) ← (0000) band. J. Quant. Spectrosc. Radiat. Transfer **57**(3), 425–434 (1997)

23. R.A. Brownsword, J.S. Salh, I.W.M. Smith, Collision Broadening of CO, Transitions in the Region of 4.3 μm. J. Chem. Soc. Faraday Trans. **91**, 5 (1995)

24. B. Khalil, F. Thibault, J. Boissoles, Argon-broadened CO_2 linewidths at high J values. Chem. Phys. Lett. **284**(3–4), 230–234 (1998)

25. C.R. Mulvihill, E.L. Petersen, High-temperature argon broadening of CO_2 near 2190 cm^{-1} in a shock tube. Appl. Phys. B **123**(10), 255 (2017)

26. G. Millot, B. Lavorel, G. Fanjoux, C. Wenger, Determination of temperature by stimulated Raman scattering of molecular nitrogen, oxygen, and carbon dioxide. Appl. Phys. B **56**(5), 287–293 (1993)

27. B. Lavorel, G. Millot, R. Saint-Loup, H. Berger, L. Bonamy, J. Bonamy, D. Robert, Study of collisional effects on band shapes of the ν_1 /$2\nu_2$ Fermi dyad in CO_2 gas with stimulated Raman spectroscopy. I. Rotational and vibrational relaxation in the $2\nu_2$ band. J. Chem. Phys. **93**(4), 2176–2184 (1990)

28. B. Lavorel, G. Millot, G. Fanjoux, R. Saint-Loup, Study of collisional effects on band shapes of the ν_1 /$2\nu_2$ Fermi dyad in CO_2 gas with stimulated Raman spectroscopy. III. Modeling of collisional narrowing and study of vibrational shifting and broadening at high temperature. J. Chem. Phys. **101**(1), 174–177 (1994)

29. R. Rodrigues, K.W. Jucks, N. Lacome, Gh. Blanquet, J. Walrand, W.A. Traub, R. Khalil, R. Le Doucen, A. Valentin, C. Camy-Peyret, L. Bonamy, J.-M. Hartmann, Model, software, and database for computation of line-mixing effects in infrared Q branches of atmospheric CO_2—I. Symmetric isotopomers. J. Quant. Spectrosc. Radiat. Transfer **61**(2), 153–184 (1999)

30. F. Thibault, J. Boissoles, C. Boulet, L. Ozanne, J.P. Bouanich, C.F. Roche, J.M. Hutson, Energy corrected sudden calculations of linewidths and line shapes based on coupled states cross sections: The test case of CO_2–argon. J. Chem. Phys. **109**(15), 6338–6345 (1998)

31. J. Lamouroux, J.-M. Hartmann, H. Tran, B. Lavorel, M. Snels, S. Stefani, G. Piccioni, Molecular dynamics simulations for CO2 spectra. IV. Collisional line-mixing in infrared and Raman bands. J. Chem. Phys. **138**(24), 244310 (2013)

32. J. Lamouroux, H. Tran, A.L. Laraia, R.R. Gamache, I.E. Gordon, J.-M. Hartmann, Updated database plus software for line-mixing in CO_2 infrared spectra and their test using laboratory spectra in the 1.5–2.3μm region. J. Quant. Spectrosc. Radiat. Transfer **111**(15), 2321–2331 (2010)

33. J. Lamouroux, L. Régalia, X. Thomas, J. Vander-Auwera, R.R. Gamache, J.-M. Hartmann, CO2 line-mixing database and software update and its tests in the 2.1 μm and 4.3 μm regions. J. Quant. Spectrosc. Radiat. Transfer **151**, 88–96 (2015)

34. J. Buldyreva, M. Chrysos, Semiclassical modeling of infrared pressure-broadened linewidths: a comparative analysis in CO_2–Ar at various temperatures. J. Chem. Phys. **115**(16), 7436–7441 (2001)

35. A. Predoi-Cross, J. Buldyreva, Characterization of line mixing effects in the 11101←00001 band of carbon dioxide for pressures up to 19 atm. J. Quant. Spectrosc. Radiat. Transfer **2021**, 107793 (2021)

36. R. Hashemi, I.E. Gordon, H. Tran, R.V. Kochanov, E.V. Karlovets, Y. Tan, J. Lamouroux, N.H. Ngo, L.S. Rothman, Revising the line-shape parameters for air- and self-broadened CO_2 lines toward a sub-percent accuracy level. J. Quant. Spectrosc. Radiat. Transfer **256**, 107283 (2020)

37. D.D. Lee, F.A. Bendana, A.P. Nair, D.I. Pineda, R.M. Spearrin, Line mixing and broadening of carbon dioxide by argon in the v3 bandhead near 4.2 μm at high temperatures and high pressures. J. Quant. Spectrosc. Radiat. Transfer **253**, 107135 (2020)

38. D.D. Lee, F.A. Bendana, A.P. Nair, S.A. Danczyk, W.A. Hargus, R.M. Spearrin, Exploiting line-mixing effects for laser absorption spectroscopy at extreme combustion pressures. Proc. Combust. Inst. **38**(1), 1685–1693 (2021)

39. A.P. Nair, D.D. Lee, D.I. Pineda, J. Kriesel, W.A. Hargus, J.W. Bennewitz, S.A. Danczyk, R.M. Spearrin, MHz laser absorption spectroscopy via diplexed RF modulation for pressure, temperature, and species in rotating detonation rocket flows. Appl. Phys. B **126**(8), 138 (2020)

40. Z. Wang, W. Wang, L. Ma, P. Fu, W. Ren, X. Chao, Mid-infrared CO_2 sensor with blended absorption features for non-uniform laminar premixed flames. Appl. Phys. B **128**(2), 31 (2022)

41. R.D. Hancock, K.E. Bertagnolli, R.P. Lucht, Nitrogen and hydrogen CARS temperature measurements in a hydrogen/air flame using a near-adiabatic flat-flame burner. Combust. Flame **109**(3), 323–331 (1997)

42. M. Gu, A. Satija, R.P. Lucht, Impact of moderate pump–Stokes chirp on femtosecond coherent anti-Stokes Raman scattering spectra. J. Raman Spectrosc. **51**(1), 115–124 (2020)

43. Z. Wang, X. Zhang, L. Xing, L. Zhang, F. Herrmann, K. Moshammer, F. Qi, K. Kohse-Höinghaus, Experimental and kinetic modeling study of the low-and intermediate-temperature oxidation of dimethyl ether. Combust. Flame **162**(4), 1113–1125 (2015)

44. T. Ombrello, Burner platform for sub-atmospheric pressure flame studies. Combust. Flame **2012**, 11 (2012)

45. T. Ombrello, C. Carter, V. Katta, Burner platform for sub-atmospheric pressure flame studies. Combust. Flame **159**(7), 2363–2373 (2012)

46. X. Liu, J.B. Jeffries, R.K. Hanson, Measurement of non-uniform temperature distributions using line-of-sight absorption spectroscopy. AIAA J. **45**(2), 411–419 (2007)

47. S. Wang, X. Liu, G. Wang, L. Xu, L. Li, Y. Liu, Z. Huang, F. Qi, High-repetition-rate burst-mode-laser diagnostics of an unconfined lean premixed swirling flame under external acoustic excitation. Appl. Opt. **58**(10), C68 (2019)

48. G. Wang, B. Mei, X. Liu, G. Zhang, Y. Li, F. Qi, Investigation on spherically expanding flame temperature of n-butane/air mixtures with tunable diode laser absorption spectroscopy. Proc. Combust. Inst. **37**(2), 1589–1596 (2019)

49. L. Rosenmann, J.M. Hartmann, M.Y. Perrin, J. Taine, Accurate calculated tabulations of IR and Raman CO_2 line broadeningby CO_2, H_2O, N_2, O_2 in the 300–2400K temperature range. Appl. Opt. **6**, 2 (2020)

50. J. Bonamy, D. Robert, C. Boulet, Simplified models for the temperature dependence of linewidths at elevated temperatures and applications to CO broadened by Ar and N_2. J. Quant. Spectrosc. Radiat. Transfer **31**(1), 23–34 (1984)

51. H.S. Lowry, C.J. Fisher, Line parameter measurements and calculations of CO broadened by H_2O and CO_2 at elevated temperatures. J. Quant. Spectrosc. Radiat. Transfer **31**(6), 575–581 (1984)

52. M. Newville, R. Otten, A. Nelson, A. Ingargiola, T. Stensitzki, D. Allan, A. Fox, F. Carter, Michał, D. Pustakhod, lneuhaus, S. Weigand, R. Osborn, Glenn, C. Deil, Mark, A. L. R. Hansen, G. Pasquevich, L. Foks, N. Zobrist, O. Frost, A. Beelen, Stuermer, kwertyops, A. Polloreno, S. Caldwell, A. Almarza, A. Persaud, B. Gamari, B. F. Maier, in *Lmfit/Lmfit-Py 1.0.2* (Zenodo, 2021)

53. D.G. Goodwin, H.K. Moffat, R.L. Speth, in Cantera: an object-oriented software toolkit for chemical kinetics, thermodynamics, and transport processes (2017)

54. H.U. Stauffer, K.A. Rahman, M.N. Slipchenko, S. Roy, J.R. Gord, T.R. Meyer, Interference-free hybrid fs/ps vibrational CARS thermometry in high-pressure flames. Opt. Lett. **43**(20), 4911 (2018)

55. D.R. Richardson, H.U. Stauffer, S. Roy, J.R. Gord, Comparison of chirped-probe-pulse and hybrid femtosecond/picosecond coherent anti-Stokes Raman scattering for combustion thermometry. Appl. Opt. **56**(11), E37–E49 (2017)

56. S. Linow, A. Dreizler, J. Janicka, E.P. Hassel, Measurement of temperature and concentration in oxy-fuel flames by Raman/Rayleigh spectroscopy. Meas. Sci. Technol. **13**(12), 1952 (2002)

57. G. Magnotti, D. Geyer, R.S. Barlow, Interference free spontaneous Raman spectroscopy for measurements in rich hydrocarbon flames. Proc. Combust. Inst. **35**(3), 3765–3772 (2015)

58. N. Jiang, S. Roy, P.S. Hsu, J.R. Gord, Direct measurement of CO_2 S-branch Raman linewidths broadened by O_2, Ar, and C_2H_4. Appl. Opt. **58**(10), C55–C60 (2019)